Building and characterizing a laser source for a 40K-MOT

Author(s):
Neubauer, Benjamin

Publication date:
2024

Permanent link:
https://doi.org/10.3929/ethz-b-000695790

ETH zürich D PHYS

Benjamin Neubauer

Building and characterizing a laser source for a ^{40}K-MOT

Semester project
Department of Physics
ETH Zürich

Supervision
Prof. Tilman Esslinger
Samuel Jele

September 19, 2024

Contents

1 Introduction

Cold atomic gases are a successful platform for studying many body quantum physics. Since the first realization of the magneto-optical trap (MOT) [1], cooling techniques have advanced and important milestones, like the Bose-Einstein-condensate [2, 3] could be reached.

The Lattice Team in the Quantum Optics group of Prof. Tilman Esslinger at ETH Zurich uses cold fermionic atoms, namely ^{40}K, to simulate the interplay of topology and interactions with great success [4, 5]. The team is currently working on a new setup, which will be able to do site resolved imaging at high repetition rates (1 Hz). Several cooling steps are necessary to get the atoms to the desired temperature for the experiment, the first of which is laser cooling in a MOT.

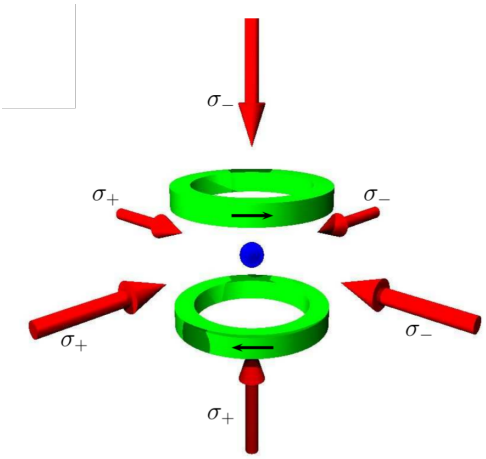

Figure 1.1: Schematic of a MOT. Three pairs of laser beams with opposite circular polarization (red) and a pair of magnetic coils in anti-Helmholtz configuration (green) cool an trap an atomic gas, such that a cloud forms at the center of the trap (blue). [6]

Figure 1.1 shows a schematic of a MOT. The six laser beams (red) exert a damping force onto the atomic gas, if they are slightly red-detuned from the $4^2S_{1/2} \rightarrow 4^2P_{3/2}$ transition of ^{40}K, called the D2-line. The magnetic coils in anti-Helmholtz configuration (green) produce an inhomogeneous magnetic field, which alters the energy of this transition through the Zeeman-effect as a function of po-

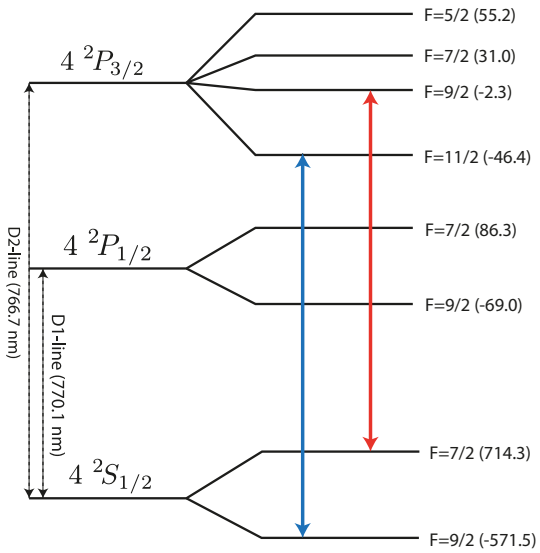

Figure 1.2: Hyperfine structure of ^{40}K. Numbers in parentheses are energy shifts with respect to the fine structure levels in units of MHz. Arrows mark the cooling (blue) and repumping (red) transitions. Values taken from [7].

sition. The result is a restoring force towards the trap center, so that at linear order, the MOT acts as a damped harmonic oscillator for the atoms. [6]

Although the atomic transition for this cooling process is chosen such that it forms a closed cycle, off-resonant excitations can cause atoms to to leave this cycle, creating the need to drive a second transition to bring these atoms back into the cooling cycle. This transition is called the repumping transition [6]. Figure 1.2 shows the level structure of ^{40}K, where these two transitions are marked in red (cooling transition at 766.7 nm) and blue (repumping transition detuned by -1.24 GHz from the cooling transtion).

The high repetition rate that is aimed for with the the setup requires fast cooling of the atoms, which in part the team wants to achieve by using larger laser beams than in traditional MOTs. To maintain the optimum laser intensity for cooling, each MOT-beam will have a power of 500 mW, yielding a total demand of 3 W of laser power for the MOT. A laser source, which provides at least 7.5 W of power is aimed for in order to accommodate for the losses through fiber couplings and a double pass AOM-arrangement for power and frequency control.

Figure 1.3 shows a schematic for the setup of the laser source. Instead of directly using a laser at the wavelength of the cooling transition (766.7 nm), we will use second harmonic generation (SHG) to double the frequency of a 1533.4 nm laser

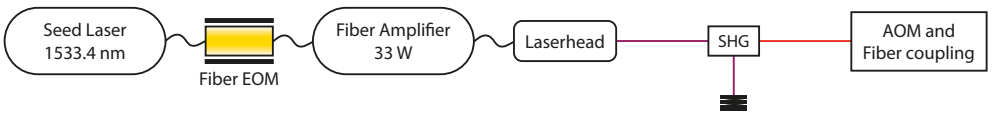

Figure 1.3: Proposed setup for the laser source.

system, consisting of seed laser, fiber amplifier and laserhead, which provides a power of 33 W. This approach is more affordable, because of the commercial availability of high power telecom wavelength lasers. It has been shown in a previous project that sufficient efficiencies can be achieved with a similar setup [8]. The fiber EOM between seed laser and amplifier will imprint sideband onto the laser spectrum, which one of them will drive the repumping transition.

This project is concerned with the assembly and alignment of the SHG-stage. chapter 2 introduces a theoretical background on SHG and gives important parameters, which will act as a starting point for experimental optimization. chapter 3 then goes on to describe the experimental setup, including the alignment procedure. chapter 4 will discuss the results concerning efficiency, beam quality, and stability. At last, chapter 5 will give a conclusion and an outlook on further steps necessary to finalize the laser source.

2 Theory of second harmonic generation

This chapter is in large parts based on Ref. [9].

Second harmonic generation is a nonlinear optical process, meaning that it originates from the nonlinear response of a medium to an applied light field. In this process, light of frequency 2ω (the second harmonic, SH) is created, as a response to an applied light field of frequency ω (the pump) in a nonlinear crystal.

The response function of nonmagnetic media is the electrical polarization $P(t)$, which can be expanded in a power series of the electric field $E(t)$:

$$P(t) = \epsilon_0 \left(\chi^{(1)} E(t) + \chi^{(2)} E^2(t) + \chi^{(3)} E^3(t) + ...\right), \tag{2.1}$$

where $\chi^{(1)}$ is the linear susceptibility and $\chi^{(2)}$, $\chi^{(3)}$ are the nonlinear susceptibilities of second, third order. SHG arises due to the presence of a second order nonlinearity, so we will only focus on this term. Given an incident electric field

$$E(t) = Ae^{-i\omega t} + A^* e^{i\omega t}, \tag{2.2}$$

with an amplitude A and a frequency ω, the second order electrical polarization is

$$P(t) = 2\epsilon_0 \chi^{(2)} |A|^2 + \epsilon_0 \chi^{(2)} \left(A^2 e^{-2i\omega t} + c.c.\right). \tag{2.3}$$

It consists of a constant term and a term oscillating at 2ω. The latter acts as a source term for electromagnetic radiation at 2ω in the wave equation derived from Maxwell's equations

$$\nabla^2 E - \frac{1}{c^2}\frac{\partial^2}{\partial t^2} E = \frac{1}{\epsilon_0 c^2}\frac{\partial^2}{\partial t^2} P, \tag{2.4}$$

which can be solved to give a condition for efficient SHG, called the phase-matching condition, which we will see in the following section.

2.1 Phase-matching

When applied to the case of SHG, Equation 2.4 gives rise to a set of coupled differential equations for the amplitudes of the pump and the SH-fields. An exact solution to these has been derived in [10], but here we will look at an approximate solution as it is more instructive. If the SHG-efficiency is low and the amplitude of the pump field does not decrease much throughout the SHG-process, the undepleted pump approximation can be applied. Then the SH-intensity scales as

$$I_{2\omega} \propto I_{\omega}^2 L^2 \operatorname{sinc}^2\left(\frac{\Delta k L}{2}\right), \tag{2.5}$$

where L is the length of the nonlinear crystal and $\Delta k = 2k_\omega - k_{2\omega}$, with k_ω and $k_{2\omega}$ the wave vectors of pump and SH, is called the phase mismatch.

The first thing to notice from this relation is that SHG is most efficient if $\Delta k = 0$, which is called the phase matching condition. This is true also in the general case without the undepleted pump approximation. The condition can be rewritten as

$$\Delta k = 2\frac{\omega}{c}\left(n(\omega) - n(2\omega)\right), \tag{2.6}$$

i.e. the phase matching condition can only be achieved if the refractive index of the medium is the same for both frequencies. For the wavelength range of our interest, the refractive index is a monotonically increasing function of frequency for all transparent media. The phase matching condition can thus only be fulfilled in birefringent media, where the SH-field is polarized along a different crystal axis than the pump field. In this project we use another method, which does not rely on birefringence: the so called quasi-phase-matching. It will be discussed in the next section.

Another thing to notice from Equation 2.5 is that the SH-intensity scales as the square of the pump intensity and the crystal length. We thus expect the SHG-efficiency $\eta = \frac{I_{2\omega}}{I_\omega}$ to scale linearly with the pump intensity. This incentivizes the use of a high power pump laser in the experiment.

Figure 2.1 shows the exact solution for pump and SH-fields as a function of propagation distance inside the crystal. The linear increase of the SH-field in the beginning is in accordance with Equation 2.5. At larger propagation distance the pump field starts to decline as more power gets converted. This causes the SH-field to saturate and the undepleted pump approximation loses its validity.

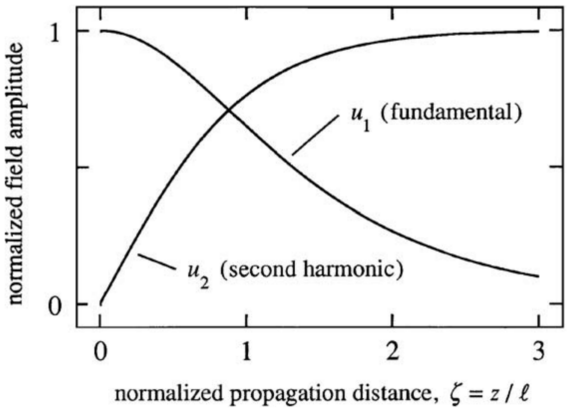

Figure 2.1: Spatial variations of the pump and SH-field amplitudes. [9]

2.2 Quasi-phase-matching

When using birefringent crystals, the phase-matching condition is usually achieved by tuning the angle of a crystal axis with respect to the propagation direction. But for angles which are not 0° nor 90°, this will cause a walk-off between the pump and the SH-beams, limiting the efficiency of the process. To avoid this walk-off, it is sometimes possible to achieve the phase matching condition by using the temperature dependence of the refractive index, while keeping the angle at 0° or 90°. Depending on the desired wavelength however, one might have to go to extreme temperatures.

One way to get around the usage of birefringence altogether is called quasi-phase-matching (QPM). In QPM, a poling period Λ is artificially introduced into the nonlinear medium. With this period the crystal orientation is inverted along the c-axis as displayed in Figure 2.2. In our case this will also be the axis along which the pump and the SH fields are polarized, since this geometry yields the largest value of $\chi^{(2)}$ [11].

Figure 2.3 shows the effect of the periodic poling. The field amplitude of the SH is plotted as a function of propagation distance in the undepleted pump approximation for three different cases. For perfect phase matching (a) we see a linear increase in the field amplitude over the length of the crystal, whereas for a wavevector mismatch (c) the field oscillates around zero. This behavior is fully described by Equation 2.5. Case (b) has the same wavevector mismatch as case (c), but the crystal is periodically poled with the same period as the oscillation in case (c). This causes the sign of $\chi^{(2)}$ to switch, when the field is at its maximum, resulting in a further increase of the field amplitude instead of the downward slope in the case without periodic poling. This way, the SH-field is able to build up and SHG efficiency is restored.

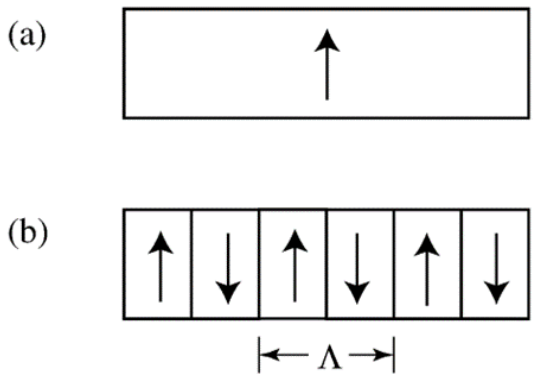

Figure 2.2: Schematic representations of a second-order nonlinear optical material in the form of (a) a homogeneous single crystal and (b) a periodically poled material, in which the crystal axis alternates in orientation with period Λ. [9]

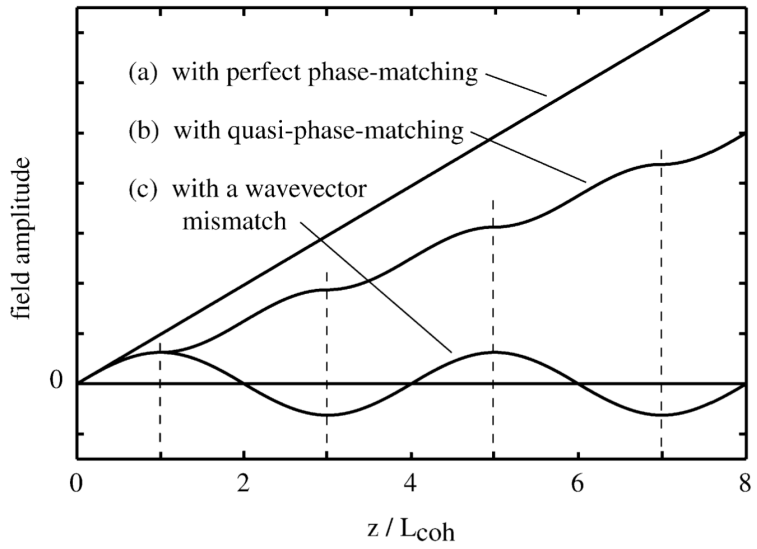

Figure 2.3: Comparison of the spatial variation of the SH-field amplitude, generated in a nonlinear optical interaction for (a) perfect phase-matching, (b) a wavevector mismatch and (c) quasi-phase-matching. [9]

In a periodically poled crystal the phase-matching condition can thus be substituted by a quasi-phase-matching condition, which includes the poling period Λ as an additional parameter:

$$\Delta k_{\mathrm{QPM}} = \Delta k - \frac{2\pi}{\Lambda} = 2\frac{\omega}{c}\left(n(\omega) - n(2\omega)\right) - \frac{2\pi}{\Lambda} = 0 \tag{2.7}$$

This new condition can be fulfilled much more easily, as the poling period can be chosen such that the condition is close to being satisfied and the temperature dependence of the refractive index can be used to fulfill the condition precisely.

2.3 Quasi-phase-matching with Gaussian beams

So far, the discussion on SHG was limited to plane waves. In the experiment however, a real laser beam is used. Therefore a Gaussian beam treatment is needed. This complicates things, because the intensity as well as the phase of the beam have nontrivial dependence on space. *Boyd and Kleinman* (BK) [12] solved this problem numerically and found values for the Rayleigh range z_R and the phase-mismatch Δk which maximize the SHG-efficiency for a given crystal length L. These are $z_R^{\mathrm{opt}} = L/5.68$ and $\Delta k^{\mathrm{opt}} = 3.2/L$ Although their work was concerned with ordinary phase matching, it can be applied to QPM by simply using the optimal value for Δk_{QPM} instead of for Δk.

2.3.1 Quasi-phase-matching temperature

The nonlinear medium used in this project is a 5%-MgO doped periodically poled lithium niobate crystal (MgO:PPLN) from *Covesion Ltd* with properties summarized in Table 2.2. The condition for quasi phase matching

$$\Delta k_{\mathrm{QPM}} - 3.2/L = 2\frac{\omega}{c}\left(n(\omega) - n(2\omega)\right) - \frac{2\pi}{\Lambda} - 3.2/L = 0, \tag{2.8}$$

can be achieved by using the temperature dependence of the refractive index. The refractive index of a medium as a function of temperature and wavelength can be approximated by the Sellmeier equation:

$$n^2(\lambda, T) = a_1 + b_1 f(T) + \frac{a_2 + b_2 f(T)}{\lambda^2 - (a_3 + b_3 f(T))^2} + \frac{a_4 + b_4 f(T)}{\lambda^2 - a_5^2} - a_6\lambda^2, \tag{2.9}$$

where $f(T) = (T - 24.5)(T + 570.82)$ is the temperature parameter with T in °C and λ in μm. The parameters $a_1, ..., a_6, b_1, ..., b_4$ for the Mgo:PPLN crystal are listed in Table 2.1. Using the crystal properties from Table 2.2 and $\lambda = 1.5334\,\mu$m,

Equation 2.8 can be solved numerically, which gives the QPM-temperature $T_{\mathrm{QPM}} = 40.59\,^{\circ}\mathrm{C}$.

a_1	a_2	a_3	a_4	a_5
5.756	0.0983	0.2020	189.32	12.52
a_6	b_1	b_2	b_3	b_4
1.32×10^{-2}	2.860×10^{-6}	4.700×10^{-8}	6.113×10^{-8}	1.516×10^{-4}

Table 2.1: Sellmeier coefficients used in Equation 2.9. Values adopted from [13].

length	30 mm	Λ	$18.9\,\mu$m
width	2 mm	$T_{\mathrm{QPM}}^{\mathrm{th}}$	$40.59\,^{\circ}$C
height	0.5 mm	$T_{\mathrm{QPM}}^{\mathrm{exp}}$	$39.87 \pm 0.03\,^{\circ}$C

Table 2.2: Properties of the 5%-MgO doped PPLN crystal. The active area of the crystal is 0.5 mm × 0.5 mm. Λ: poling period, $T_{\mathrm{QPM}}^{\mathrm{th}}$: theoretically predicted QPM-temperature, $T_{\mathrm{QPM}}^{\mathrm{exp}}$: experimentally found QMP-temperature (subsection 4.1.2).

2.3.2 Boyd-Kleinman focusing formula

For efficient SHG, the pump beam needs to be focused into the crystal to reach high intensity. The best SHG-efficieny is achieved, if the condition $z_R^{\mathrm{opt}} = L/5.68$ is met. A more useful quantity than z_R is the waist radius w_0. Using the relation $z_R = \frac{\pi w_0^2 n(\lambda, T_{\mathrm{QPM}})}{\lambda}$ we can immediately calculate the optimal waist according to the Boyd-Kleinman focusing formula:

$$w_{\mathrm{BK}} = \sqrt{\frac{L\lambda}{\pi n(\lambda, T_{\mathrm{QPM}}) \times 5.68}} = 34.8\,\mu\mathrm{m}. \tag{2.10}$$

The values for w_{BK} and T_{QPM} calculated in this section will act as a starting point for the experimental setup and will then be optimized.

3 Experimental setup

This setup uses SHG in a nonlinear crystal to obtain resonant light for the ^{40}K-MOT at 766.7 nm from a pump laser at 1533.4 nm. Figure 3.1 shows a sketch of the setup.

The laser system described in section 3.1 produces the pump beam with linear polarization and a power of 33 W at 1533.4 nm. The combination of half-wave plate (L/2) and polarizing beam splitter (PBS) adjusts the fraction of laser power used for SHG. This is useful for aligning the setup (section 3.3), where low laser power should be used for safety reasons.

The next set of elements prepare the beam for optimal conversion efficiency in the nonlinear crystal. To get the highest value of the nonlinear susceptibility, another half-wave plate (L/2) is needed to rotate the p-polarized light transmitted by the PBS to point along the periodically poled crystal axis (section 2.2). The lenses L1 ($f = -50$ mm) and L2 ($f = 100$ mm) are selected such that the focus of the beam inside the crystal can be adjusted to different waist sizes in proximity to the BK-waist (Equation 2.10) by tuning the position of L1. Tuning the waist of the focus will also shift its position, which is why the position of the crystal stage is also adjustable. The crystal stage will be described in more detail in section 3.2.

To collimate the SH-beam after the crystal, a lens with $f = 75$ mm (L3) with Thorlabs B-coating is used. This coating allows a high transmission for the SH-beam, but has no positive effect on the transmission of the pump beam. The latter is not ideal, as a power of a few watts will be reflected at L3, and will thus not be dumped in a controlled manner. This light is however unlikely to cause any damage on components, since the beam is divergent.

A dichroic mirror separates the two colors, transmitting the SH-beam and dumping the remaining pump beam.

An aluminum enclusore designed in Ref. [8] minimizes dust deposition onto the optics and isolates the crystal stage from any variations in air flow. It is indicated by the light grey shaded region. The three laser beams can enter/leave the box through AR-coated windows. A photograph of the setup is shown in Figure 3.2.

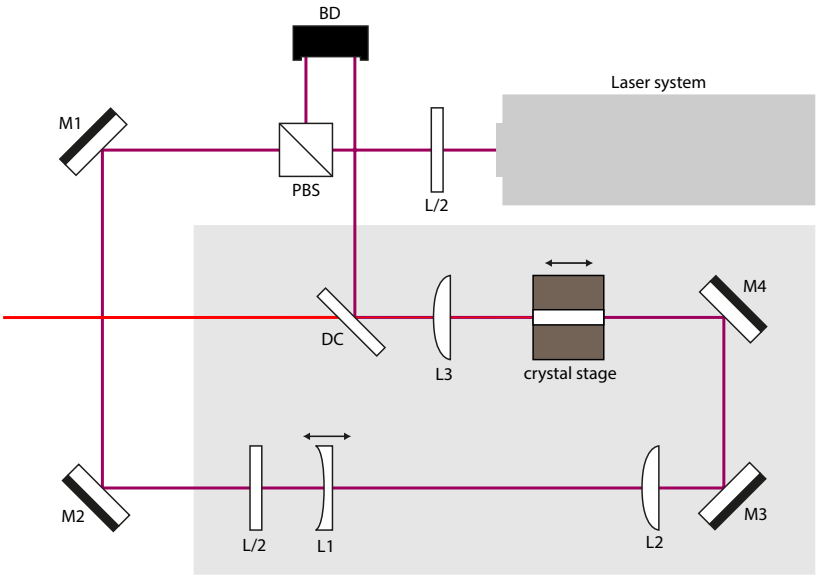

Figure 3.1: Sketch of the SHG-setup. L/2: half-wave plate, PBS: polarizing beam splitter, BD: beam dump, M1-M4: dielectric mirrors, L1: concave lens ($f = -50\,\mathrm{mm}$), L2: convex lens ($f = 100\,\mathrm{mm}$), L3: convex lens ($f = 75\,\mathrm{mm}$), DC: dichroic mirror, crystal stage: nonlinear crystal mounted on a peltier element and temperature sensor for temperature control. Beam waist inside the crystal is determined by the position of L1 and crystal stage (indicated by arrows over these elements). The light grey area: aluminum enclosure.

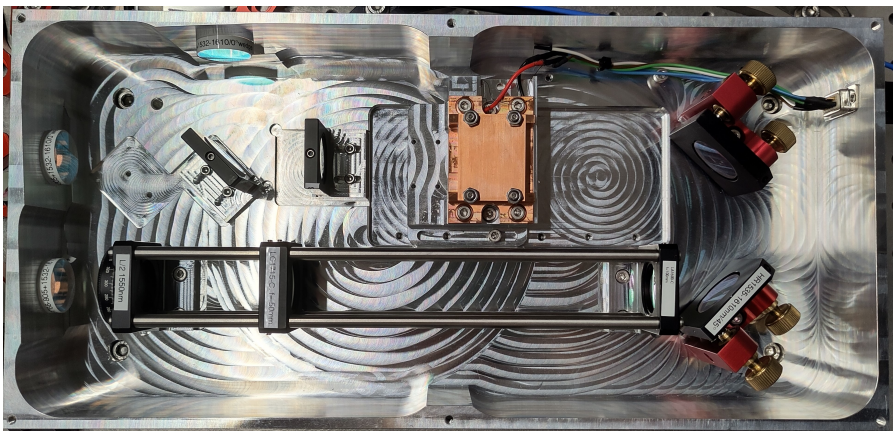

Figure 3.2: Photograph of the setup inside the aluminum enclosure

3.1 The pump beam

The laser system used for the pump beam consist of a seed laser by *NKT Photonics* and a fiber amplifier by *Precilasers*. Between these two, a fiber EOM will later be installed, which is responsible for the driving the repumping transition. This is however not part of this project.

The fiber amplifier can be run with an amplification current from 0 to 27.5 A, yielding a laser power of 0 to 35 W. We will always run the amplifier with a current of 26 A, which will give about 33 W of laser power, and tune the power going to the experiment with the waveplate-beamsplitter combination. This has the advantage of not changing the beam shape when changing the power.

A calibration measurement, shown in Figure 3.3, is carried out. The laser power going to the beam dump was measured as a function of waveplate angle with the thermal powerhead *S322C* from *Thorlabs*, which has a $\pm 5\,\%$ uncertainty. A fit of the form

$$P_{\text{fit}} = a\cos^2\left(2(\phi - b)\right) + d \tag{3.1}$$

was performed on the data, where P_{fit} is the power, ϕ is the waveplate angle, and a, b, d are parameters to be determined in the fit. The values, which best fit the data are $a = 32.4 \pm 0.4\,\text{W}$, $b = -8.59 \pm 0.06\,^\circ$ and $d = 0.229 \pm 0.007\,\text{W}$. The nonzero value of d is not due to an imperfection of the PBS, but rather due to the nature of the powerhead, which is made for measuring powers from 0.1 W to 200 W. The power going to the experiment is thus taken to be

$$P_{\text{in}} = a - (P_{\text{fit}} - d) = a\sin^2\left(2(\phi - b)\right). \tag{3.2}$$

In order to calculate the beam waist inside the crystal, it is necessary to know the beam parameters of the pump. Because of the lack of a camera for this wavelength, these were not measured, but instead taken from the manual. It specifies a focal beam waist of $w_{\text{pump}} = 0.685\,\text{mm}$ at a distance $z = 473\,\text{mm}$ from the output and a divergence angle of $\theta_0 = 713\,\text{mrad}$. The waist inside the crystal is then calculated with the software *GaussianBeam* using these values and the focal lengths of lenses L1 and L2. As we will see in section 4.1, this calculation probably did not give a very precise estimate of the real waist.

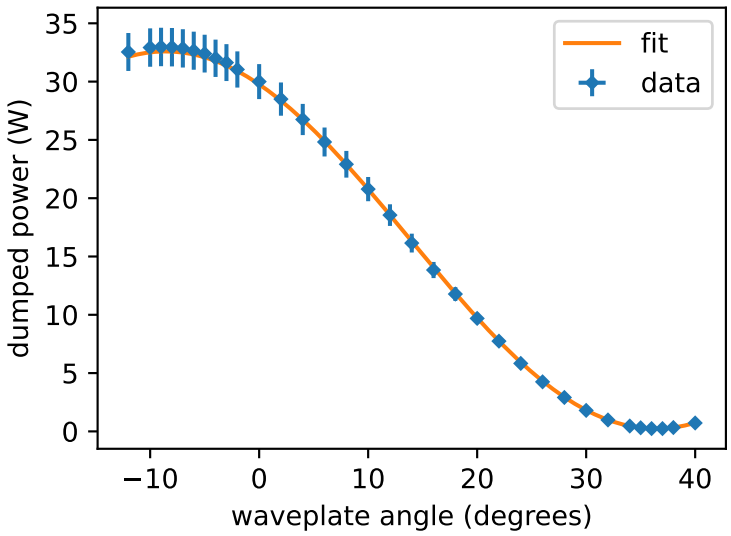

Figure 3.3: Calibration of waveplate angle to laser power. Errorbars are a 5 % uncertainty.

3.2 The crystal stage

The properties of the nonlinear MgO:PPLN crystal are summarized in Table 2.2. Its temperature is stabilized with the *TEC-1161-4A-NTC* temperature controller by *Meerstetter engineering*, in order to achieve the QPM-temperature.

Figure 3.4 shows a photograph of the crystal stage. The crystal (1) is mounted into a copper housing for good thermal conductivity. A piece of 100 μm thick indium foil ensures good thermal contact with the copper pieces. The temperature of the housing is measured with a 10 kΩ NTC temperature sensor[1]. For this, a hole of 1 mm diameter is drilled into the housing following the direction of the arrow of (2), but at the center of the crystal. A Peltier element[2] (3) heats the crystal to its QPM-temperature. An aluminum slider (4) allows to move to crystal, such that the pump beam is centered at its focus.

During the experiment the temperature of the crystal is kept constant within 0.005 °C.

[1] B57551G1103F005 - Thermistor NTC 10kOhm 3612K 73.3mm, *EPCOS*
[2] RND 460-00145 - Peltier Element 72W 8A 16.3V, 40x40mm, *RND*

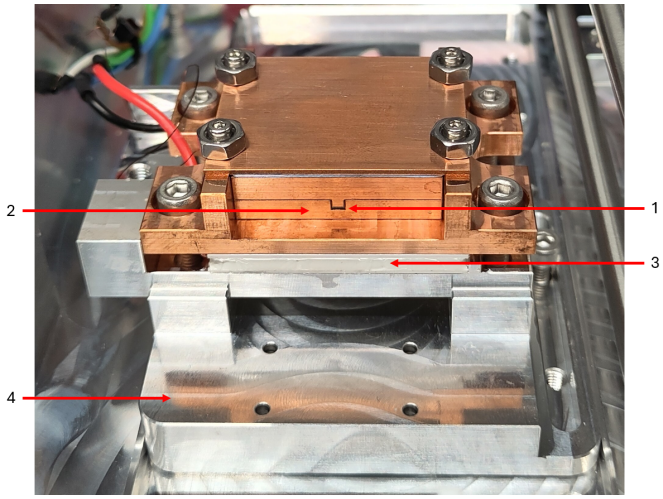

Figure 3.4: Photograph of the crystal stage. (1) Location of the crystal, (2) location of the temperature sensor (at the center of the crystal), (3) Peltier element, (4) aluminum slider.

3.3 Alignment of the setup

To ensure good SHG-efficiency and especially good beam quality, the system needs to be aligned precisely. Here we describe the alignment procedure step by step. The waveplate-beamsplitter combination was already set up when the project was started, so we skip this step.

Aligning to the lens system We start by setting the laser power to around 100 mW and remove all components from the aluminum enclosure. The two mirrors M1 and M2 align the laser beam to the cage system. For this, an iris is mounted to each end-piece of the cage. We measure the transmitted power, optimize it by beamwalking and diminish the aperture for the next iteration. When the laser beam is nicely aligned, we remove the irises and mount again all components.

Aligning to the crystal The alignment of the beam to the crystal is more challenging than the first step, as it is not sufficient to optimize to a power measurement. We can divide the procedure into two steps. The first goal is to get any SH-signal and to maximize the power of this signal. This usually gives a bad beam profile, which is why we use a camera in the second step to make sure the beam propagates through the center of the crystal

First step We start by setting the focal waist to the BK-waist by positioning L1 accordingly. Before the crystal stage is inserted, we use an iris on an aluminum

slide, whose aperture is at the same position as the aperture of the crystal stage. We use the mirrors M3 and M4 to make sure, the laser beam is aligned to this iris at all positions on the slide.

We now insert the crystal stage and move it, such that its center is at the focal position. This can be estimated with an IR-card. We set the temperature to the QPM-temperature and use a photodiode based power-head to detect SH-light at 766.7 nm.

We should now already see a small SH-signal, which we optimize by beam walking. Here it is not important to find the exact maximum, but just to be close to a maximum, i.e. the power should not change much when slightly turning the screws.

Second step We now use a camera to look at the beam profile. For this we need to turn up the power to around 1 W, because the PBS distorts the pump beam shape if the transmitted power is set too low. The SH-signal is too strong to put directly onto the camera, so a reflection from a glass plate is used instead, while dumping the main part of the SH-beam.

In most cases, we now need to beam walk by a surprisingly large amount. The goal is to walk the beam to a position, where it behaves symmetrically, when moving it out of the active aperture with the screws of M4. So to be clear, when using the vertical screw of M4, it should look similar, when moving the beam out to the top as moving it out to the bottom. And when using the horizontal screw of M4, it should look similar, when moving the beam out to the left as moving it out to the right. It is generally not possible to align one pair of screws after the other, as the vertical screws also slightly affect the horizontal position of the beam and vice versa. It is therefore necessary to alternate between the pairs until the goal is reached.

The beam now propagates through the center of the crystal and should be very resilient against any drifts, which might slightly alter the beam path. On top of that, it should have a Gaussian profile, which may be slightly elliptical.

Collimation of the beam The last step of the alignment procedure is the collimation of the SH-beam. For this we choose the focal length $f = 75\,\text{mm}$ for L3, which gives us a beam diameter of around 1.2 mm, when collimated. This diameter is chosen, such that the beam still fits through the AOM-arrangement and couples well to the fibers.

The procedure for finding the position of L3, which collimates the beam, is described in section 4.2 as it involves several measurements.

4 Experimental results

The goal of the experiment is to maximize the efficiency of SHG (section 4.1), while maintaining a good beam quality (section 4.2) and stability (section 4.3). Apart from aligning the system well (section 3.3), we have two parameters to maximize the efficiency, which are the waist (subsection 4.1.1) and the temperature (subsection 4.1.2).

4.1 Efficiency results

4.1.1 Effect of the waist size

Here we present the main results of this work, which is the dependence of the SHG-efficiency on the pump power for several waist sizes. We set the waist size by adjusting the positions of the lenses L1 and L2 in Figure 3.1. Note that the system might have to be realigned after changing the lens positions. The values of the waists given here, are inferred as described at the end of section 3.1. Values for lens positions and inferred waists are listed in Table 4.1.

$w_0\,(\mu\mathrm{m})$	38.6	34.9	31.9	29.6	25.9	23.0
$d_{L1}\,(\mathrm{mm})$	38	38	38	29	11	
$d_{L2}\,(\mathrm{mm})$	186	196	206	206	206	
$d_{L1}\,(\mathrm{mm})$				56	38	18
$d_{L2}\,(\mathrm{mm})$				233	233	233

Table 4.1: Lens positions, used to set the waist (first row) in the first (second row) and second round (third row) of measurements. The distances d_{L1} and d_{L2} are measured from the right side of the left end piece of the cage system to the left side of the respective mounts of L1 and L2. Compare Figure 3.2 for a photo of the setup.

Two rounds of measurements were carried out, because there had to be made minor changes to the setup after the first round. In both rounds, the efficiency η is determined by measuring the SH-power $P_{2\omega}$ as a function of the fundamental power P_ω and then calculating $\eta = P_{2\omega}/P_\omega$. For each waist, the first three data

points of $P_{2\omega}$ were measured with the power head *S130C* by *Thorlabs*, which is made for a power range of 500 pW to 500 mW, and has an uncertainty of $\pm 3\,\%$. The rest was measured with the same power head as in the calibration measurement (see section 3.1). P_ω was set by adjusting the waveplate angle and using the calibration curve (Equation 3.2). For each data point, the temperature was adjusted to maximize the SH-power.

First round of measurements chapter 3 describes the final setup, which is accurate for the second round of measurements. The differences to this final setup in the first round of measurements are the following:

- L3 had a focal length of 150 mm and a thorlabs C-coating, which is not suitable for the wavelength of the SH-beam.
- L2 was not mounted in the end piece of the cage system, but rather an movable element in the cage. This was changed together with the focal length of L3, to collimate the beam to the desired waist.
- AR-coated windows shown in Figure 3.2 were not yet implemented.

Figure 4.1 shows the data obtained in the first round of measurements. We determined the SHG-efficiency as a function of input power for 5 different waist sizes, including the BK-waist, shown in orange.

From Equation 2.5 we expect a linear dependence on pump power$\eta \propto P_\omega$, as long as the undepleted pump approximation is valid. We assume this is the case if $\eta \lesssim 10\,\%$ and thus perform a linear fit onto the first four data points for each waist, indicated by a dashed line of corresponding color. The determined slopes are listed in Table 4.2.

Firstly, we notice that in all cases the initial slope is not maintained. One reason for this is pump depletion, i.e. the pump intensity gets weaker while propagating the crystal, because a significant amount is converted to SH-radiation. Another reason could be that absorption might start to play a role at high pump power. This would introduce a temperature gradient in the crystal, giving rise to a phase-mismatch, again limiting the efficiency.

A second thing to notice is that the waist, which achieved the largest initial slope, plotted in purple color, maintained the highest efficiency across all input powers.

The inset shows the maximum efficiency achieved for each waist. We notice that the BK-waist was not close to achieving the maximum efficiency, but instead a much smaller waist. As we will discuss, this was likely due to a poor estimate of the waist size. The waists plotted in red and purple achieved similar efficiencies, potentially indicating proximity to a maximum.

The overall maximum efficiency is $\eta_{\max,1} = 24.1 \pm 1.3\,\%$ corresponding to a power of $P_{2\omega}^{\max,1} = 7.8 \pm 0.4\,\mathrm{W}$, with an initial slope of $0.92 \pm 0.12\,\frac{\%}{\mathrm{W}}$. This result is just above our goal of 7.5 W of SH-power, but the error tells us that we might have not achieved it yet.

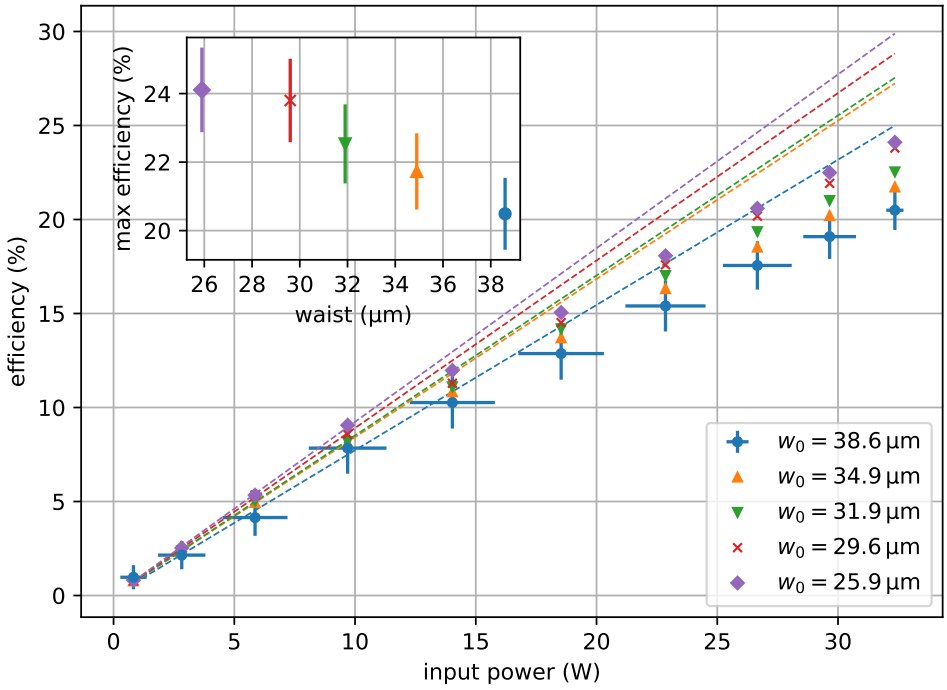

Figure 4.1: SHG-efficiency as a function for five waist sizes in the first round of measurements. Linear fits are performed onto the first four data points for each waist (dashed lines), where the undepleted pump approximation is valid. At higher intput power, these slopes are not maintained by the data, indicating pump depletion. Errorbars are due to uncertainties of fit parameters from Equation 3.1 and error propagation due to an assumed uncertainty of 0.2° in the waveplate angle. They are only shown for one waist for better visibility. The inset shows the maximum efficiency for each waist.

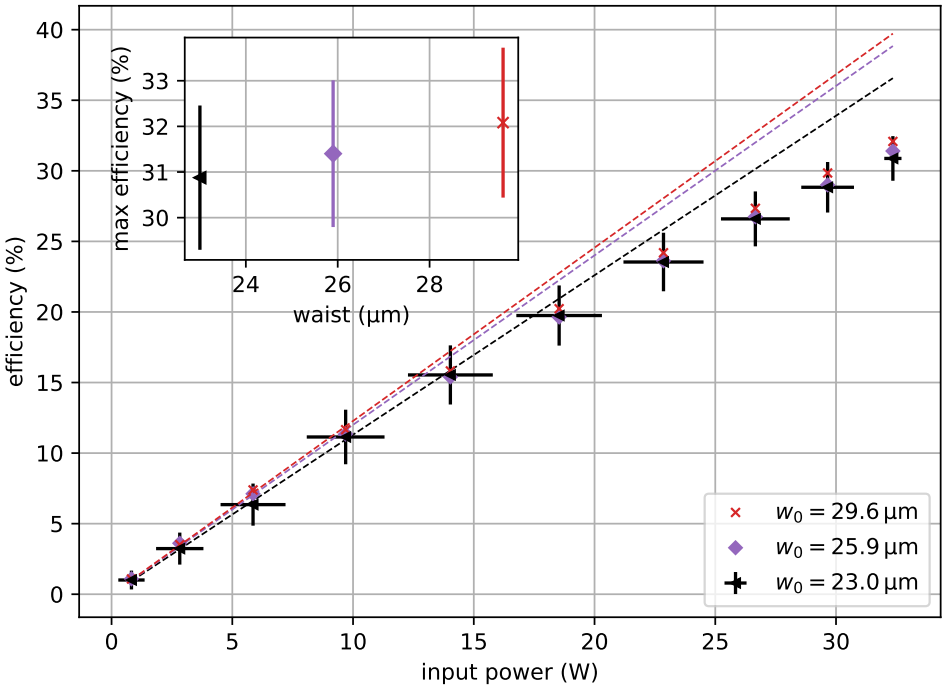

Figure 4.2: SHG-efficiency as a function for three waist sizes in the second round of measurements. Dashed lines, errorbars and inset similar to Figure 4.1.

Second round of measurements Figure 4.2 shows the data taken, when the experimental setup was in its final state as described in chapter 3. We chose to carry out the measurement at the waist, which performed the best in the first round (purple), and for one smaller (black) and one larger waist (red).

The results are quite similar, but there are two main differences.

Firstly, the maximum efficiency $\eta_{\max,2} = 32.1 \pm 1.7\%$ corresponding to a power of $P_{2\omega}^{\max,2} = 10.4 \pm 0.6\,\mathrm{W}$, as well as the initial slope of $1.23 \pm 0.16\,\frac{\%}{\mathrm{W}}$, are much larger than in the first round. The differences between the two setups, which could influence the measured SH-power are the different coating on L3 and potentially a different quality of alignment. With this result, we certainly reached the goal which we set in the introduction (chapter 1).

Secondly, the maximum efficiency was reached by the waist plotted in red, which performed worse than the waist plotted in purple in the first round. This difference in performance is however much smaller than the uncertainty.

Again, the initial slopes are listed in Table 4.2.

Discussion of the results Here we want to compare the results of this work to a similar project by Samuel Jele [8], who used the setup to double the frequency of a 1064 nm pump beam to get a 532 nm SH-beam for an optical lattice.

Samuel Jele was able to achieve an overall higher initial slope of 2.07 %/W and maximum efficiency of 40.6 % at a pump power of 34.8 W, than in this work. Also, his data shows a much stronger saturation and almost a plateau in efficiency at high input power. The highest initial slope was achieved by the BK-waist, but the maximum efficiency was achieved by a larger waist, which showed a smaller initial slope but less saturation at high power.

The overall higher efficiency in his work can be explained by the difference in wavelength, which comes with different SHG-efficiency. The strong saturation, and especially the fact that the saturation could be reduced by choosing a larger waist, hint at strong thermal effects, i.e. absorption in the crystal. In this work absorption seems to play much less of a role.

Another major difference between the two works, is that Samuel Jele was able to measure the waist at the focus, while we only inferred it in this work. He achieved the highest initial slope for the BK-waist, which is exactly what BK predict, while we measured the highest initial slope for a much smaller waist. This is a hint, that our calculation for the waist is very likely inaccurate.

38.6	34.9	31.9	29.6	25.9	23.0
0.77 ± 0.10	0.84 ± 0.11	0.85 ± 0.11	0.89 ± 0.12	0.92 ± 0.12	
			1.23 ± 0.16	1.20 ± 0.16	1.13 ± 0.15

Table 4.2: Slopes of linear fits from Figure 4.1 and Figure 4.2. First row: waist w_0 in μm. Second row: Slopes from the first round of measurements in %/W. Third row: Slopes from the second round of measurements in %/W.

4.1.2 Temperature dependence

Another parameter which influences the SHG-efficiency is the crystal temperature. Here we look at the temperature dependence of the SHG-efficiency with a waist of $w_0 = 29.6\,\mu$m (red data points in previous subsection). Figure 4.3 shows the temperature dependence of the SH-power at maximum pump power. The data (blue) was taken with the power monitoring setup described in subsection 4.3.2. The orange curve shows the theoretical prediction in the undepleted pump approximation (Equation 2.5). It was shifted from having its maximum at $T_{\mathrm{QPM}}^{\mathrm{th}} = 40.59\,^{\circ}\mathrm{C}$ (dark grey), which is the theoretically predicted QPM-temperature, to fit the data best. This was the case for $T_{\mathrm{QPM}}^{\mathrm{exp}} = 39.87 \pm 0.03\,^{\circ}\mathrm{C}$ (light grey).

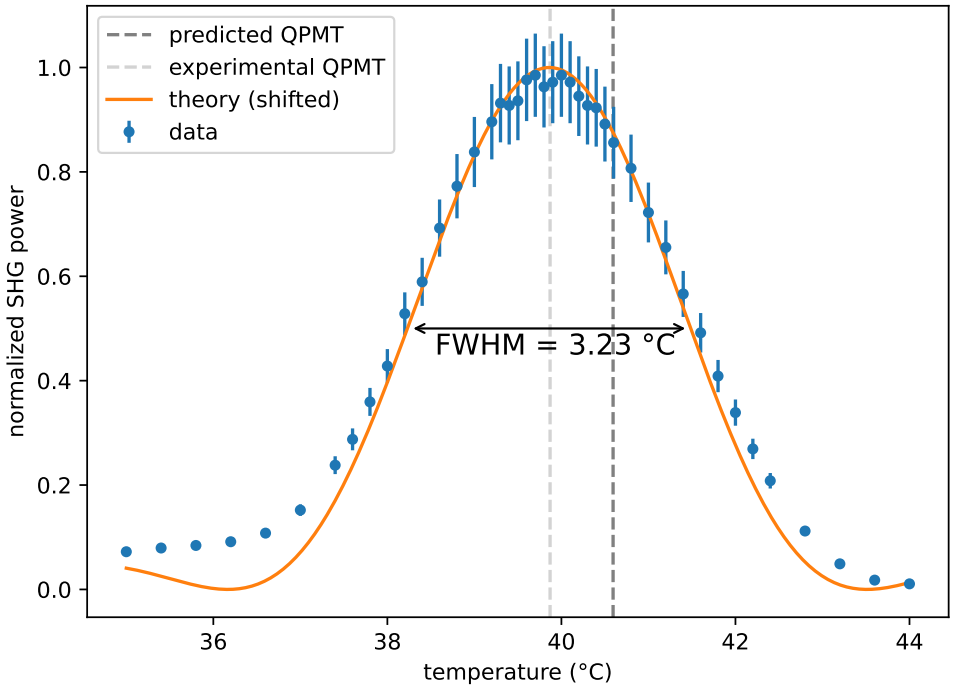

Figure 4.3: Temperature dependence of SH-power for maximum pump power and a waist of $w_0 = 29.6\,\mu$m (blue), and theoretical prediction from Equation 2.5 (orange), shifted from the predicted QPM-temperature (dark grey) to fit the experimentally determined maximum (light grey). Errorbars are due to errors in fit parameters from subsection 4.3.2

Although the undepleted pump approximation is not valid here, the data fit the theory quite well. The theory predicts a temperature bandwidth of 3.23 °C at FWHM, which seems to be accurate.

The difference in predicted and determined QPM-temperature can have multiple reasons. Firstly, it could result from imprecise manufacturing of the periodic poling. Covesion state in their data sheet [14], that actual values might vary from the calculated phase matching temperatures. In this case however the reason for the observed difference is absorption, which is a heating source for the crystal. To compensate for this, the set point of the controller has to be decreased to achieve the correct QPM-temperature. Looking at the temperature which maximized the efficiency for each pump power, plotted in Figure 4.4, we see that indeed for low pump power, the ideal temperature is very close to the predicted QPM-temperature, but decreases for larger pump powers.

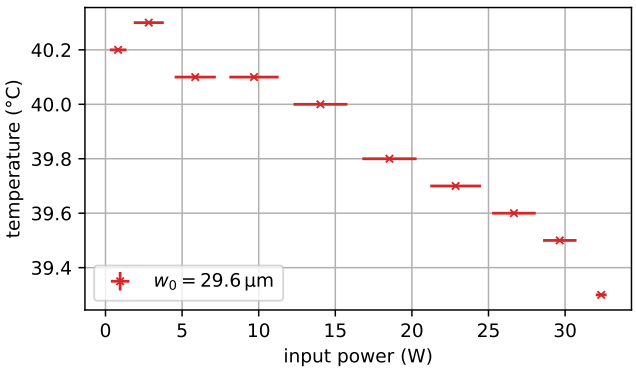

Figure 4.4: Temperatures used for achieving the SH-powers plotted in red in Figure 4.2.

4.2 Colimmation of the beam

When the beam leaves the SHG-stage, it should be collimated to a waist which is small enough to fit through the AOM-arrangement, while still being large enough to ensure a small divergence angle. We choose a waist radius of about $w_0 = 0.6\,\text{mm}$, which gives us a Rayleigh range of about $z_R = 1.5\,\text{m}$.

To collimate the beam we fist use a *Shack-Hartmann wavefront sensor* from *Thorlabs*, which can measure the radius of curvature of the beam's wavefront. We move the lens L3 to a position which maximizes the radius of curvature.

Starting from this position, we measure the beam waist at several distances from the lens. For this we use a camera and fit a Gaussian profile onto each image which gives two values of waists w_1 and w_2 along the principle axes. We repeat the process for two more lens positions. The results are shown in Figure 4.5. The average waist is calculated as $\bar{w} = \sqrt{w_1 w_2}$. The distances, given in the legend, are with respect to the position of L3 after using the wavefront sensor. The least divergence is observed for the blue data points, i.e. the collimation was improved by moving L3 by 2 mm from the previous position.

We will keep the lens at this position and record the beam waist two more times at several distances from L3. The three measurements are shown in Figure 4.6 in different colors. In order to determine the beam waist w_0 and position z_0, a fit of the form

$$w(z) = w_o \sqrt{1 + \left(\frac{z - z_0}{z_R}\right)^2}, \tag{4.1}$$

is performed. The result is $w_0 = 585 \pm 6\,\mu\text{m}$ at a distance $z_0 = 417 \pm 29\,\text{mm}$ from L3. This waist is equivalent to a Rayleigh range of $z_R = 1402 \pm 25\,\text{mm}$.

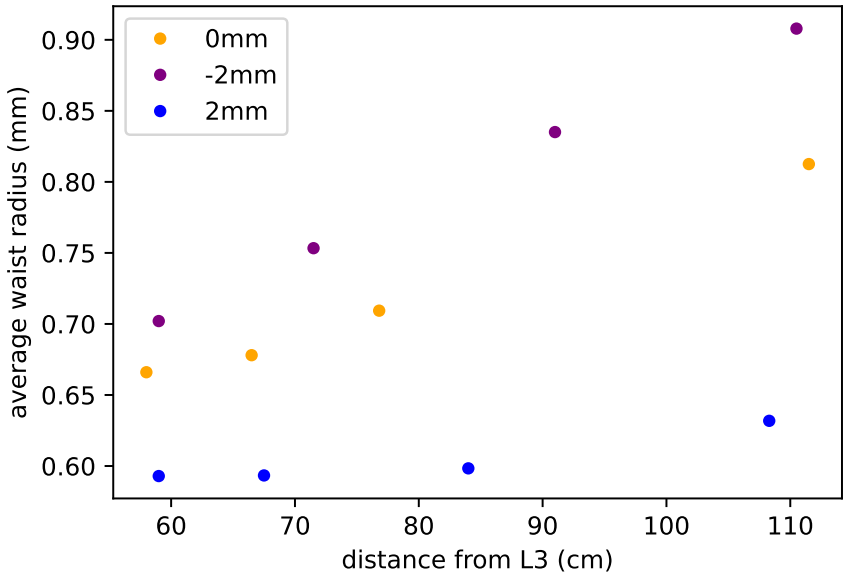

Figure 4.5: Average waist radius of the SH-beam as a function distance from L3 for three different positions of L3. Positions are given with respect to the position after using the wavefront sensor.

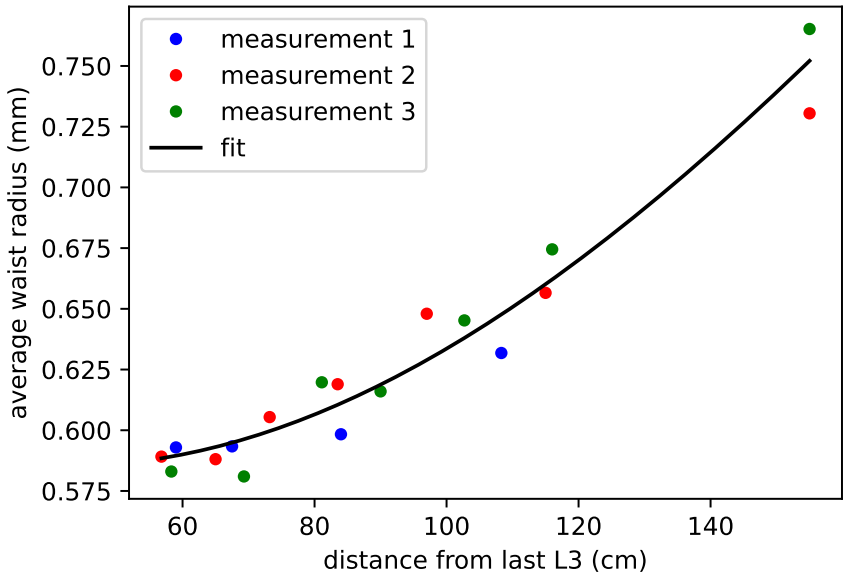

Figure 4.6: Three measurements of average beam waist for the final position of L3. Equation 4.1 is fit to the data, yielding a waist of $w_0 = 585 \pm 6\,\mu$m at a distance $z_0 = 417 \pm 29\,$mm from L3.

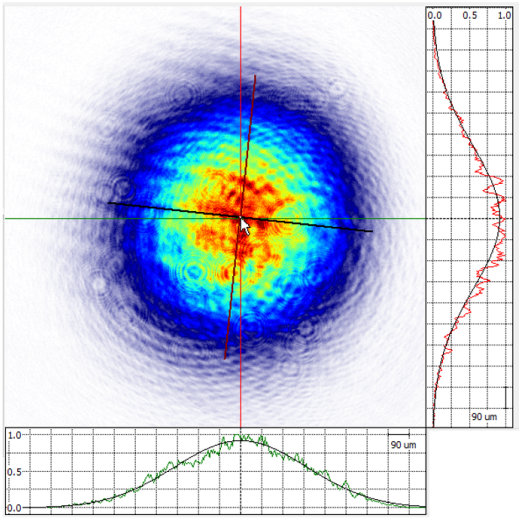

(a) Distance from L3: 65 cm. $w_1 = 567\,\mu$m, $w_2 = 611\,\mu$m. Elipticity $\frac{w_1}{w_2} = 0.928$.

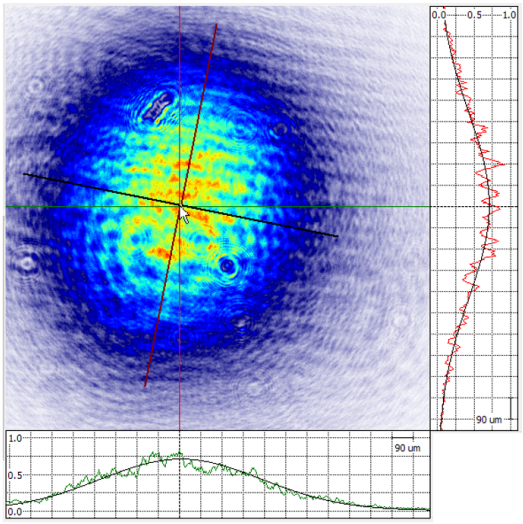

(b) Distance from L3: 155 cm. $w_1 = 682\,\mu$m, $w_2 = 783\,\mu$m. Elipticity $\frac{w_1}{w_2} = 0.871$.

Figure 4.7: Two beam profiles from measurement 2 at different distances from L3. Gaussian fits are performed, which yield waist radii w_1 (along black line) and w_2 (along red line).

Figure 4.7 shows examples of beam profiles at two distances from L3. Both images are recorded as part of measurement 2. As expected, the beam gets larger, when moving further away from L3. On top of that, we see that the second beam is more elliptical than the first one. This could hint at a slight astigmatism of the beam.

4.3 Stability of the system

4.3.1 Long term measurement

To guarantee a stable performance of the MOT, it is crucial, that the power of the SH-beam drifts little time. Here we measure its power over almost three hours. This measurement was carried out after the first round of measurements of efficiencies, with the waist, which performed the best ($w_0 = 25.9\,\mu$m).

Figure 4.8 shows the SH-power as a function of time. We label the power at zero minutes with 100 %, which is 7.42 W. In the first 40 minutes the power decreases to 99 %, which is 7.36 W, and subsequently increases over two hours to 102 %, which is 7.57 W. Although these drifts are not huge, it is still nice to constantly keep

track of them, which is why we install a power monitoring for the SH-beam.

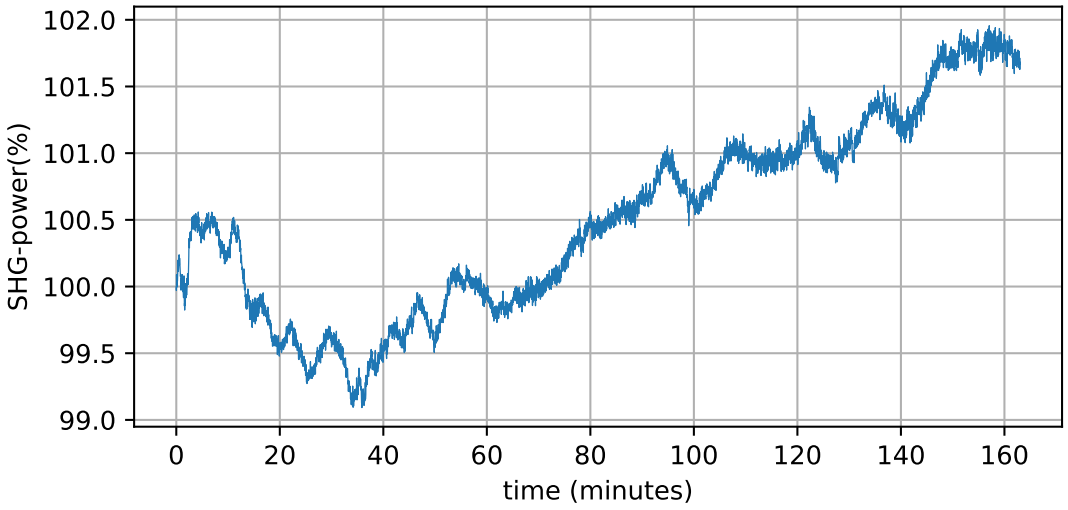

Figure 4.8: SH-power measured over almost three hours. The power at zero minutes is 7.42 W, which we label with 100 %.

4.3.2 Power monitoring

Figure 4.9 shows the setup of the power monitoring. As the beam leaves the SHG-stage (1), less then one percent of its power is reflected at an AR-coated window (2). This reflection is then sent onto a photo diode (4) via a mirror (3). The photo diode measures a voltage, which is proportional to the power of the light hitting it.

To determine the proportionality constant, a calibration measurement, shown in Figure 4.10, is performed. We measure the power of the SH-beam with the power head for several waveplate angles and simultaneously record the voltage on the photo diode. A linear fit gives a slope of $m = 4.71 \pm 0.09 \,\frac{\mathrm{W}}{\mathrm{V}}$ and an offset of $t = 8 \pm 21\,\mathrm{mW}$.

A similar monitoring would also be desirable for the pump beam, to look for correlations in the power drifts of the two beams. This will be installed in the future, when a suitable photo diode for the pump wavelength is available.

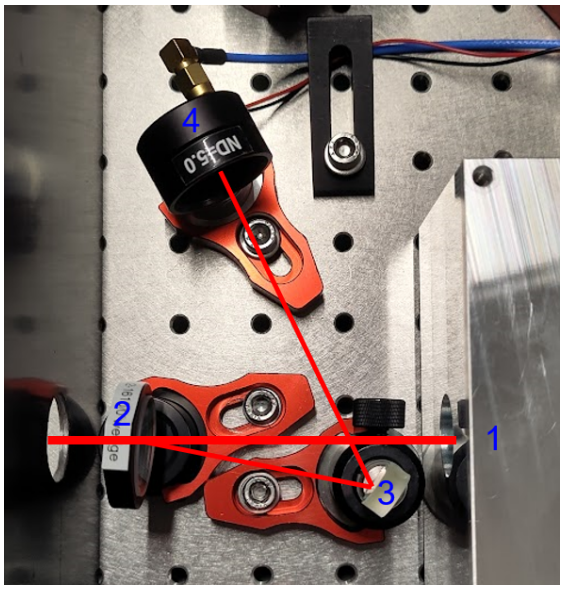

Figure 4.9: Power monitoring setup. (1): exit of the SHG-stage, (2): AR-coated window, (3): mirror, (4): photo diode.

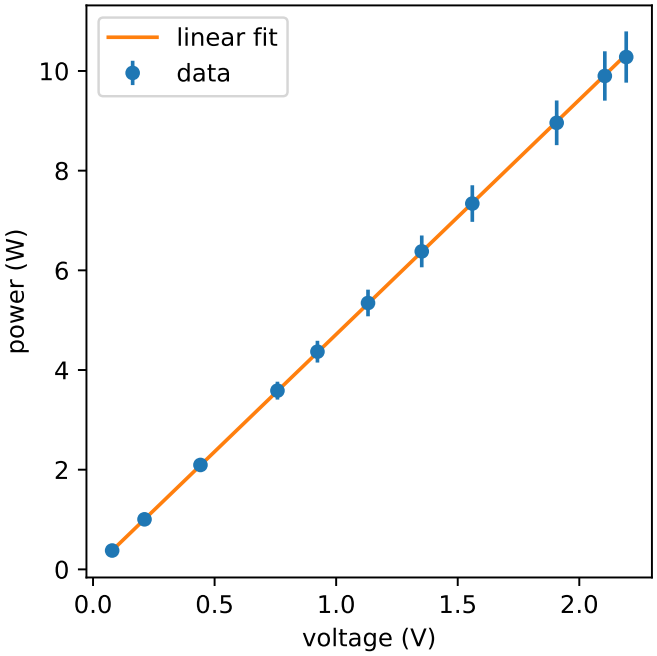

Figure 4.10: Calibration of the power monitoring. Blue: Power measured with the powerhead vs. voltage on the photo diode. Orange: Linear fit to the data.

5 Conclusion

The goal of this project was to build and characterize a stable laser source for a ^{40}K-MOT at 766.7 nm using second harmonic generation. To meet the requirements of the MOT, the laser source needed a power of at least 7.5 W and a good beam shape.

In chapter 2 we briefly introduced a theoretical background on SHG, which allowed us to calculate the beam waist and crystal temperature, which maximize the SHG-efficiency.

After that, chapter 3 was concerned with the details of the setup and explained the alignment procedure in detail.

Starting from the theoretical optimal values calculated in chapter 2, we tried to optimize the SHG-efficiency experimentally in chapter 4. We noticed, that the waist, which optimized the efficiency, was far off the theoretical prediction. By comparison to a previous project [8], we concluded, that this was due to our inability of measuring the waist. The calculated optimal temperature however could be confirmed at low pump power, and needed to be adjusted at high pump power, due to absorption. With these optimizations, we were able to achieve a power of 10.4 ± 0.6 W at a good beam quality, achieving the goal of this project.

Further steps need to be taken, before the laser source can be used for the MOT.

Double pass AOM arrangements for frequency and power control will be installed. With these the observed drifts in laser power can be compensated, and the cooled ^{40}K-cloud can be moved into the next chamber for further cooling steps.

On top of that, the fiber EOM needs to be installed to produce side bands, which drive the repumping transition. The interaction between this phase modulation and subsequent SHG needs to be tested. Theoretically, choosing a certain modulation depth can lead to the destructive interference of the carrier frequency after SHG [15]. This is desirable at the end of cooling, where only optical pumping should be active.

At last, the same laser source needs to be built at 780 nm in order to cool ^{87}Rb-atoms, which are required for further cooling steps of the ^{40}K-atoms.

Acknowledgments

First, I would like to thank Prof. Esslinger and Prof. Donner, for giving me the opportunity to conduct this project in their group and for sparking my interest in their research topic with an excellent lecture on Quantum Optics. I am also very grateful to the members of the lattice team; Dr. Konrad Viehbahn for the trust to let me work on this crucial part of the experiment, Samuel Jele for his close supervision and for always taking the time to listen to my concerns, Marius Gächter for sharing his experiences of working in science for multiple years, and Giacomo Bisson for his helpful assistance in the laboratory.

Bibliography

[1] E. L. Raab, M. Prentiss, A. Cable, S. Chu, and D. E. Pritchard, "Trapping of neutral sodium atoms with radiation pressure," *Phys. Rev. Lett.*, vol. 59, pp. 2631–2634, Dec 1987.

[2] M. H. Anderson, J. R. Ensher, M. R. Matthews, C. E. Wieman, and E. A. Cornell, "Observation of bose-einstein condensation in a dilute atomic vapor," *Science*, vol. 269, no. 5221, pp. 198–201, 1995.

[3] K. B. Davis, M. O. Mewes, M. R. Andrews, N. J. van Druten, D. S. Durfee, D. M. Kurn, and W. Ketterle, "Bose-einstein condensation in a gas of sodium atoms," *Phys. Rev. Lett.*, vol. 75, pp. 3969–3973, Nov 1995.

[4] A.-S. Walter, Z. Zhu, M. Gächter, J. Minguzzi, S. Roschinski, K. Sandholzer, K. Viebahn, and T. Esslinger, "Quantization and its breakdown in a hubbard–thouless pump," *Nature Physics*, vol. 19, no. 10, pp. 1471–1475, 2023.

[5] Z. Zhu, M. Gächter, A.-S. Walter, K. Viebahn, and T. Esslinger, "Reversal of quantized hall drifts at noninteracting and interacting topological boundaries," *Science*, vol. 384, no. 6693, pp. 317–320, 2024.

[6] C. Cohen-tannoudji and D. Guery-odelin, *Advances In Atomic Physics: An Overview*. World Scientific Publishing Company, 2011.

[7] T. Tiecke, "Properties of potassium," *University of Amsterdam, The Netherlands, Thesis*, 2010.

[8] S. Jele, "Engineering optical lattices in k-space," *ETH Zurich, Switzerland, Thesis*, 2023.

[9] R. Boyd, *Nonlinear Optics*. Elsevier Science, 2003.

[10] J. A. Armstrong, N. Bloembergen, J. Ducuing, and P. S. Pershan, "Interactions between light waves in a nonlinear dielectric," *Phys. Rev.*, vol. 127, pp. 1918–1939, Sep 1962.

[11] I. Shoji, T. Kondo, A. Kitamoto, M. Shirane, and R. Ito, "Absolute scale of second-order nonlinear-optical coefficients," *J. Opt. Soc. Am. B*, vol. 14, pp. 2268–2294, Sep 1997.

[12] G. D. Boyd and D. A. Kleinman, "Parametric Interaction of Focused Gaussian Light Beams," *Journal of Applied Physics*, vol. 39, pp. 3597–3639, 07 1968.

[13] O. Gayer, Z. Sacks, E. Galun, and A. Arie, "Temperature and wavelength dependent refractive index equations for mgo-doped congruent and stoichiometric linbo 3," *Applied Physics B*, vol. 91, pp. 343–348, 2008.

[14] Covesion Ltd, Unit A7, The Premier Centre, Premier Way, Romsey, SO51 9DG, UK, *Device Specification MSHG1550-0.5-xx*, 5th ed., 2021. Available at https://covesion.com/wp-content/uploads/2021/08/MSHG1550-0.5-v5.0-bleeds.pdf.

[15] C. M. Holland, Y. Lu, and L. W. Cheuk, "Synthesizing optical spectra using computer-generated holography techniques," *New Journal of Physics*, vol. 23, no. 3, p. 033028, 2021.